

connecting the p40 "anchoring helix" to Arp3 may allow this reorientation.

Much more work is required to determine how Arp2/3 complex is activated and mediates filament branching. The crystal structure of Arp2/3 complex provides the foundation for detailed analysis of these mechanisms as well as more penetrating studies of actin filament dynamics in cells.

#### References and Notes

- L. M. Machesky, S. J. Atkinson, C. Ampe, J. Vandekerckhove, T. D. Pollard, *J. Cell Biol.* **127**, 107 (1994).
- T. M. Svitkina, A. B. Verkhovskiy, K. M. McQuade, G. G. Borisy, *J. Cell Biol.* **139**, 397 (1997).
- T. M. Svitkina, G. G. Borisy, *J. Cell Biol.* **145**, 1009 (1999).
- R. D. Mullins, J. A. Heuser, T. D. Pollard, *Proc. Natl. Acad. Sci. U.S.A.* **95**, 6181 (1998).
- L. Blanchoin et al., *Nature* **404**, 1007 (2000).
- K. J. Amann, T. D. Pollard, *Nature Cell Biol.* **3**, 306 (2001).
- L. M. Machesky et al., *Proc. Natl. Acad. Sci. U.S.A.* **96**, 3739 (1999).
- R. Rohatgi et al., *Cell* **97**, 221 (1999).
- D. Winter, T. Lechler, R. Li, *Curr. Biol.* **9**, 501 (1999).
- D. Yarar, W. To, A. Abo, M. D. Welch, *Curr. Biol.* **9**, 555 (1999).
- C. Egile et al., *J. Cell Biol.* **146**, 1319 (1999).
- T. D. Pollard, L. Blanchoin, R. D. Mullins, *Annu. Rev. Biophys. Biomol. Struct.* **29**, 545 (2000).
- H. N. Higgs, T. D. Pollard, *Annu. Rev. Biochem.* **70**, 649 (2001).
- J. B. Marchand, D. A. Kaiser, T. D. Pollard, H. N. Higgs, *Nature Cell Biol.* **3**, 76 (2001).
- L. M. Machesky, R. H. Insall, *Curr. Biol.* **8**, 1347 (1998).
- H. Miki, T. Takenawa, *Biochem. Biophys. Res. Commun.* **243**, 73 (1998).
- L. M. Machesky et al., *Biochem. J.* **328**, 105 (1997).
- M. D. Welch, A. H. DePace, S. Verma, A. Iwamatsu, T. J. Mitchiner, *J. Cell Biol.* **138**, 375 (1997).
- J. F. Kelleher, S. J. Atkinson, T. D. Pollard, *J. Cell Biol.* **131**, 385 (1995).
- R. D. Mullins, W. F. Stafford, T. D. Pollard, *J. Cell Biol.* **136**, 331 (1997).
- N. Volkman et al., *Science* **293**, 2456 (2001).
- R. D. Mullins, T. D. Pollard, *Curr. Opin. Struct. Biol.* **9**, 244 (1999).
- For supplemental information, see Science Online ([www.sciencemag.org/cgi/content/full/294/5547/1679/DC1](http://www.sciencemag.org/cgi/content/full/294/5547/1679/DC1)).
- D. C. Winter, E. Y. Choe, R. Li, *Proc. Natl. Acad. Sci. U.S.A.* **96**, 7288 (1999).
- The arrangement of subunits agrees well with the following contacts identified by chemical cross-linking: Arp3 to p34, p21, and p20; Arp2 to p40 and p34 (long linker); p40 to p34; and p20 to p16 (long linker). It also agrees with a two-hybrid interaction, p34 to p20 (75).
- The residues of Arp2 that interact with ATP in actin are highly conserved in Arp2: actin Asp<sup>154</sup> = Arp2 Asp<sup>158</sup>, Asp<sup>157</sup> = Asp<sup>161</sup>, Gly<sup>158</sup> = Gly<sup>162</sup>, Val<sup>159</sup> = Val<sup>163</sup>, Lys<sup>213</sup> = Lys<sup>217</sup>, Glu<sup>214</sup> = Glu<sup>218</sup>, Gly<sup>301</sup> = Gly<sup>306</sup>, Thr<sup>302</sup> = Ser<sup>307</sup>, Met<sup>304</sup> = Met<sup>309</sup>, and Tyr<sup>305</sup> = Tyr<sup>310</sup>. The residues of Arp3 that interact with ATP in actin are also highly conserved: actin Asp<sup>11</sup> = Arp3 Asp<sup>11</sup>, Ser<sup>14</sup> = Thr<sup>14</sup>, Gly<sup>15</sup> = Gly<sup>15</sup>, Leu<sup>16</sup> = Tyr<sup>16</sup>, Lys<sup>18</sup> = Lys<sup>18</sup>, Asp<sup>154</sup> = Asp<sup>169</sup>, Asp<sup>157</sup> = Asp<sup>172</sup>, Gly<sup>158</sup> = Gly<sup>173</sup>, Val<sup>159</sup> = Val<sup>174</sup>, Lys<sup>213</sup> = Lys<sup>228</sup>, Glu<sup>214</sup> = Glu<sup>229</sup>, Gly<sup>301</sup> = Gly<sup>324</sup>, Thr<sup>302</sup> = Ser<sup>325</sup>, Met<sup>304</sup> = Met<sup>327</sup>, Tyr<sup>305</sup> = Phe<sup>328</sup>, and Lys<sup>336</sup> = Arg<sup>374</sup>.
- M. J. Dayel, E. A. Holleran, R. D. Mullins, *Proc. Natl. Acad. Sci. U.S.A.*, in press.
- The following residues contribute to the interface between the COOH-terminal helices of p34 and p20: p34 Leu<sup>243</sup>, Phe<sup>247</sup>, Tyr<sup>250</sup>, His<sup>254</sup>, Ser<sup>258</sup>, Tyr<sup>261</sup>/Ile<sup>262</sup>, Phe<sup>273</sup>, Val<sup>276</sup>/Leu<sup>277</sup>; p20 Phe<sup>134</sup>, His<sup>137</sup>, Met<sup>149</sup>, Ser<sup>152</sup>, Arg<sup>156</sup>, Val<sup>160</sup>, and Phe<sup>164</sup>. Two salt bridges between the helices are p34 Arg<sup>265</sup>-p20 Glu<sup>145</sup> and p34 Lys<sup>296</sup>-p20 Glu<sup>141</sup>. Rather than a 3-4-3-4-3-4 pattern, the pattern of interface residues is 4-3-4-4-3-4-3-4-3 in p34 and 3-4-4-3-4-4-4 in p20. Two interface residue pairs of p34 (Tyr<sup>261</sup>/Ile<sup>262</sup> and Val<sup>276</sup>/Leu<sup>277</sup>) straddle the p20 chain.
- H. N. Higgs, L. Blanchoin, T. D. Pollard, *Biochemistry* **38**, 15212 (1999).
- D. Pantaloni, R. Boujemaa, D. Didry, P. Gounon, M.-F. Carlier, *Nature Cell Biol.* **2**, 385 (2000).
- J. Zalesky, I. Grigorova, R. D. Mullins, *J. Biol. Chem.* **276**, 3468 (2001).
- M. Bailly et al., *Curr. Biol.* **11**, 620 (2001).
- P. J. McLaughlin, J. T. Gooch, H. G. Mannherz, A. G. Weeds, *Nature* **364**, 685 (1993).
- R. C. Robinson et al., *Science* **286**, 1939 (1999).
- C. E. Schutt, J. C. Myslik, M. D. Rozycki, N. C. Goonesekere, U. Lindberg, *Nature* **365**, 810 (1993).
- Collaborative Computational Project No. 4, *Acta Crystallogr. D* **50**, 760 (1994).
- T. A. Jones, J. Y. Zou, S. W. Cowan, M. Kjeldgaard, *Acta Crystallogr. A* **47**, 100 (1991).
- A. Perrakis, T. K. Sixma, K. Wilson, V. S. Lamzin, *Acta Crystallogr. D* **53**, 448 (1997).
- E. La Fortelle, G. Bricogne, *Methods Enzymol.* **276**, 472 (1997).
- DINO: Visualizing Structural Biology (2001) ([www.dino3d.org](http://www.dino3d.org)).
- P. J. Kraulis, *J. Appl. Crystallogr.* **24**, 946 (1991).
- Persistence of Vision Raytracer (1997) ([www.povray.org](http://www.povray.org)).
- A. Nicholls, K. A. Sharp, B. Honig, *Proteins Struct. Funct. Genet.* **11**, 281 (1991).
- The coordinates are deposited in the Protein Data Bank (PDB) (accession number 1K8K). We thank W. Kwiatkowski for help with the illustrations and computer systems, D. Davies of NIH for providing hospitality for K.T. in Maryland, and K. Amann, E. Andrianantoandro, and C. Beltzner for helpful suggestions on the text. Supported by NIH research grants GM-26132 and GM-26338 (T.P.) and GM-56653 (S.C.), a Pioneer Foundation Fellowship (R.R.), an NRSA Fellowship (H.H.), and the Human Frontier Science Program.

18 September 2001; accepted 25 October 2001

## REPORTS

# Self-Assembly and Mineralization of Peptide-Amphiphile Nanofibers

Jeffrey D. Hartgerink, Elia Beniash, Samuel I. Stupp\*

We have used the pH-induced self-assembly of a peptide-amphiphile to make a nanostructured fibrous scaffold reminiscent of extracellular matrix. The design of this peptide-amphiphile allows the nanofibers to be reversibly cross-linked to enhance or decrease their structural integrity. After cross-linking, the fibers are able to direct mineralization of hydroxyapatite to form a composite material in which the crystallographic *c* axes of hydroxyapatite are aligned with the long axes of the fibers. This alignment is the same as that observed between collagen fibrils and hydroxyapatite crystals in bone.

Self-assembly and biomineralization are used in biology for fabrication of many composite materials. Bone tissue is a particularly com-

plex example of such a composite because it contains multiple levels of hierarchical organization (1). At the lowest level of this hierarchy is the organization of collagen fibrils with respect to hydroxyapatite (HA) crystals. The collagen fibrils are formed by self-assembly of collagen triple helices and the HA crystals grow within these fibrils in such a way that their *c* axes are oriented along the long axes of the fibrils (2). The preparation of

any material with structure on the nanoscale is a challenging problem. Fabrication of materials that resemble bone, even at the lowest level of hierarchical organization, is even more difficult because it involves two dissimilar organic and inorganic nanophases that have a specific spatial relation with respect to one another. One way to accomplish this in an artificial system is to prepare an organic nanophase designed to exert control over crystal nucleation and growth of the inorganic component.

The controlled nucleation and growth of crystals from organic templates has been demonstrated by in vitro experiments (3–8) and in a number of natural biomineralizing systems (9–11). These studies on templated crystal growth suggest that nucleation occurs on surfaces which expose repetitive patterns of anionic groups. These anionic groups tend to concentrate the inorganic cations creating local supersaturation followed by oriented nucleation of the crystal. Many groups have investigated the preparation of bone-like materials with the use of organic substrates such as poly(lactic acid), reconstituted collagen, and many others (12–18), and some studies show a similar correlation between the crys-

Department of Materials Science and Engineering, Department of Chemistry, and Medical School, Northwestern University, 2225 North Campus Drive, Evanston, IL 60208, USA.

\*To whom correspondence should be addressed. E-mail: s-stupp@northwestern.edu

tallographic orientation of hydroxyapatite when the organic scaffold is made from reconstituted collagen (19). However, to our knowledge, this has never been demonstrated in a designed self-assembling system.

We report on the use of self-assembly and mineralization to prepare a nanostructured composite material that recreates the structural orientation between collagen and hydroxyapatite observed in bone. The composite is prepared by self-assembly, covalent capture, and mineralization of a peptide-amphiphile (PA). The PA is synthesized by standard solid phase chemistry that ends with the alkylation of the  $\text{NH}_2$  terminus of the peptide. Mono or di-alkyl tails attached to the  $\text{NH}_2$  or  $\text{COOH}$  termini of peptides have been reported to influence their aggregation and secondary structure in water in both synthetic (20–22) and natural (23) systems. According to existing knowledge of amphiphile self-assembly (24), an alkyl tail with 16 carbon atoms coupled to an ionic peptide should create an amphiphile that assembles in water into cylindrical micelles because of the amphiphile's overall conical shape. The alkyl tails would pack in the center of the micelle leaving the peptide segments exposed to the aqueous environment. These cylindrical micelles can be viewed as fibers in which the chemistry of the peptide region is repetitively displayed on their surface.

Three features were engineered into the peptide region of the PA. First, the prepared fibers must be robust, and for this reason four consecutive cysteine amino acids were incorporated in the sequence for covalent capture (25–30) of the supramolecular nanofibers. These residues can be used to form disulfide bonds between adjacent molecules upon oxidation, which lock the supramolecular structure into place. The formation of the disulfide bonds is reversible, allowing either self-correction of improper disulfide bonds or a return to the supramolecular structure by treatment with mild reducing agents. Second, the fibers must be able to nucleate the formation of HA in the proper environment. It is well known that acidic moieties play a key role in biomineralization processes (11, 12) and that phosphorylated groups are particularly important in the formation of calcium phosphate minerals. For example in dentin, the phosphophoryn protein family contains numerous repeats of the sequences Asp-Ser(P)-Ser(P) and Ser(P)-Asp (31). These massively phosphorylated proteins are closely associated with the collagen extracellular matrix (ECM) and are known to play an important role in HA mineralization (32). Therefore, we incorporated a phosphoserine residue into the peptide sequence that, after self-assembly, allows the fiber to display a highly phosphorylated surface equivalent to that presented by a long peptide segment. This, in part, captures the

repetitive organization of phosphate groups found in phosphophoryn proteins. Third, it would be beneficial for biomedical applications if the fibers could promote the adhesion and growth of cells on their surfaces. Another collagen-associated protein, fibronectin, contains the sequence Arg-Gly-Asp (RGD). This sequence has been found to play an important role in integrin-mediated cell adhesion (33); therefore, we included RGD in our peptide as well. Collectively, these design principles led us to prepare the PA molecule shown in Fig. 1.

After synthesis, the PA (34) was treated with dithiothreitol (DTT) at a pH of 8 to

reduce all cysteine residues to free thiols. At this pH, the PA was found to be soluble in excess of 50 mg/ml in water. However, upon acidification of the solution below pH 4, the material rapidly becomes insoluble. Solutions more concentrated than 2.5 mg/ml form birefringent gels in water that are self-supporting upon inversion of the container. Examination of the gels by cryo-transmission electron microscopy (cryo-TEM), which preserves the native, hydrated state of the material, revealed a network of fibers with a diameter of  $7.6 \pm 1$  nm (35, 36) and lengths up to several micrometers (Fig. 2B). Positively and negatively stained dried fibers were found to have

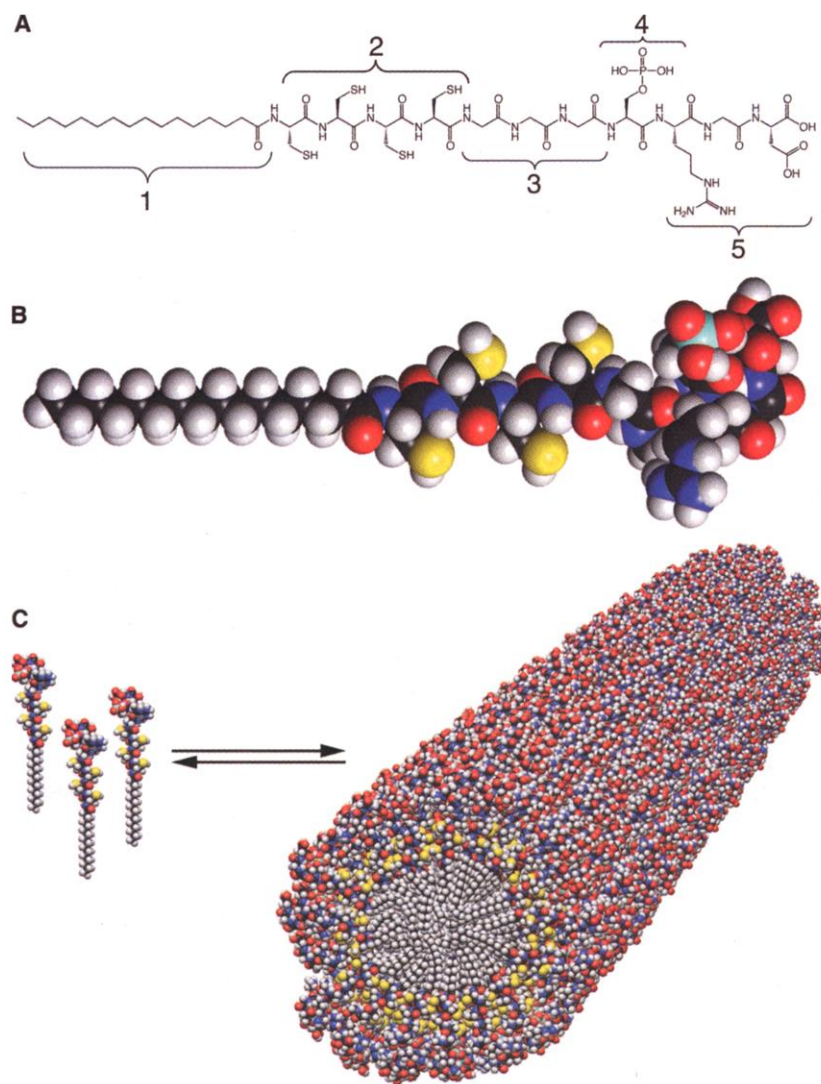


**Fig. 1.** (A) Chemical structure of the peptide amphiphile, highlighting five key structural features. Region 1 is a long alkyl tail that conveys hydrophobic character to the molecule and, when combined with the peptide region, makes the molecule amphiphilic. Region 2 is composed of four consecutive cysteine residues that when oxidized may form disulfide bonds to polymerize the self-assembled structure. Region 3 is a flexible linker region of three glycine residues to provide the hydrophilic head group flexibility from the more rigid cross-linked region. Region 4 is a single phosphorylated serine residue that is designed to interact strongly with calcium ions and help direct mineralization of hydroxyapatite. Region 5 displays the cell adhesion ligand RGD. (B) Molecular model of the PA showing the overall conical shape of the molecule going from the narrow hydrophobic tail to the bulkier peptide region. Color scheme: C, black; H, white; O, red; N, blue; P, cyan; S, yellow. (C) Schematic showing the self-assembly of PA molecules into a cylindrical micelle.

diameters of  $6.0 \pm 1$  nm (Fig. 2, A and C). When TEM was used with the positive stain uranyl acetate, which preferentially stains acidic groups (37), it revealed increased electron density at the periphery of the fiber. Additionally, gels that were stained, embedded in epoxy resin, and sectioned for TEM, showed fibers in cross section in which donut-shaped patterns were observed, indicating that only the outer portion of the fiber stained (Fig. 2D). These two positive-staining experiments indicate that the hydrophobic alkyl tails pack on the inside of the fiber and the acidic moieties of the peptide are displayed on the surface of the fiber. The formation of the fibers was found to be concentration-independent over more than three orders of magnitude (0.01 mg/ml to 50 mg/ml); however, a second level of hierarchy was observed that was concentration-dependent. As the concentration of the PA was increased, a larger number of the fibers were observed to pack into flat ribbons of fibers (Fig. 2, A and C). Examination of the self-assembled material by Fourier transform infrared spectroscopy (FTIR) revealed a bimodal amide I peak with maxima at  $1658\text{ cm}^{-1}$  ( $\alpha$  helix) and  $1632\text{ cm}^{-1}$  ( $\beta$  sheet) along with a N-H stretching peak at  $3287\text{ cm}^{-1}$ , indicating the formation of a hydrogen bonded structure, possibly using a combination of  $\beta$  sheet and  $\alpha$  helical secondary structure in the fibers (38, 39). On the basis of the above data, the nanofibers were modeled as cylindrical micelles in which the alkyl tails pack on the inside of the fiber and peptide segments are displayed on the outside in the form of both  $\beta$  sheet and  $\alpha$  helical secondary structures. This model results in a fiber with a diameter of 8.5 nm, which is within the margin of error of our TEM measurements (Fig. 1C).

When the pH is lowered below 4 with HCl, the material self-assembles; when the pH is brought back to neutral with KOH, it disassembles. This pH-triggered self-assembly and gelation allows the material to respond to its environment and, thus, may have applications in controlled release of molecules (40). After self-assembly of PA molecules into fibers, the cysteine thiol groups were oxidized by treatment with 0.01 M iodine. Examination of the material by TEM reveals that the fibers remain intact (Fig. 2, C and D). These oxidized PA fibers were found to be stable to alkaline solutions (pH 8) for months, whereas fibers that had not been oxidized would disassemble within min. On the basis of the length of the fibers revealed by TEM and our model for the molecular organization of the fibers, this yields a polymer with a molecular weight of roughly  $2 \times 10^8$  daltons. The covalent capture process can be easily reversed by treating the fibers with a mild reducing agent such as DTT. After reduction, the fibers regain their pH sensitiv-

**Fig. 2.** (A) Negative stain (phosphotungstic acid) TEM of the self-assembled nanofibers before covalent capture. Fibers are arranged in ribbon-like parallel arrays. (B) Vitreous ice cryo-TEM of the fibers in their native hydrated state to be  $7.6 \pm 1$  nm. (C) Positive stain (uranyl acetate) TEM of the self-assembled nanofibers after oxidative cross-linking shows electron dense regions due to the stain that localized on the periphery of the fibers. (D) Thin section TEM of positively stained (uranyl acetate) nanofibers after oxidative cross-linking and embedding in epoxy resin. Two fibers are observed in cross section (arrows), showing the lack of staining in the interior of the fiber.

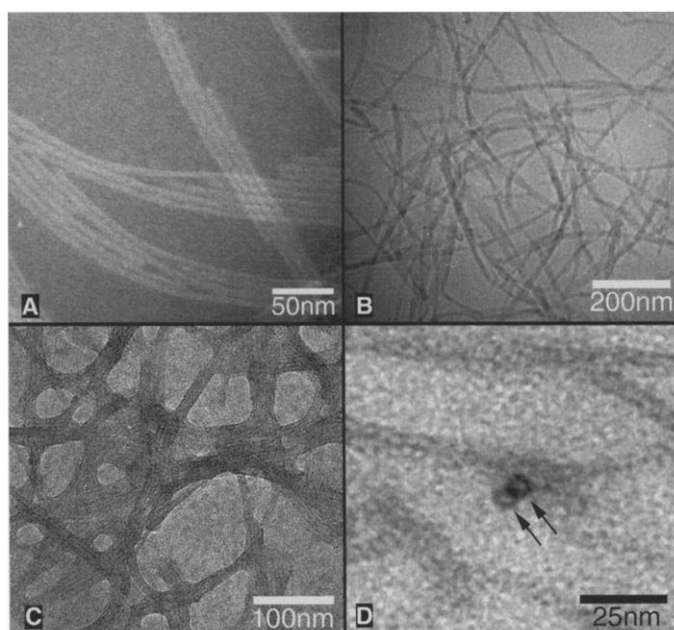
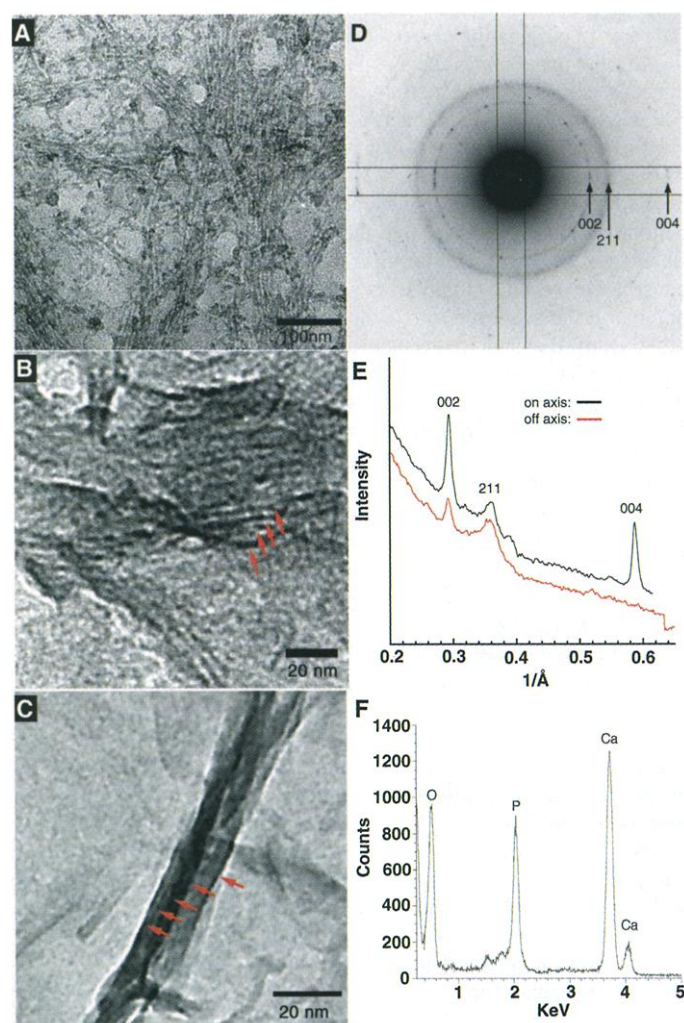


**Fig. 3.** (A) TEM micrographs of the unstained, cross-linked peptide-amphiphile fibers incubated for 10 min in  $\text{CaCl}_2$  and  $\text{Na}_2\text{HPO}_4$  solution. The fibers arranged in bundles are visible due to the high concentration of inorganic ions on their surface. (B) After 20 min, forming HA crystals (red arrows) are observed in parallel arrays on some of the PA fibers. (C) After 30 min, mature HA crystals (red arrows) completely cover the PA fibers. (D) Electron diffraction pattern taken from a mineralized bundle of PA fibers after 30 min of exposure to calcium and phosphate. The presence and orientation of the diffraction arcs corresponding to the 002 and 004 planes (whose intensities are enhanced with respect to the 211 family of reflections) indicate preferential alignment of the crystals along their *c* axes along the long axis of the bundle. (E) Plot of intensity versus inverse angstroms reveals that the 002 and 004 peaks of hydroxyapatite are strongly enhanced along the peptide-amphiphile fiber axis. (F) EDS profile of mineral crystals after 30 min of incubation reveals a Ca/P ratio of  $1.67 \pm 0.08$ , as expected for HA.



ity and rapidly disassemble at pH 8. Together with the controlled self-assembly, this creates a highly dynamic system that can interconvert between discrete molecules, self-assembled supramolecular fibers, and covalently captured polymeric fibers, depending solely on the environment in which the material is placed.

To investigate the mineralization properties of the PA nanofibers, the material was assembled and mineralized directly on a holey, carbon-coated TEM grid. This approach allows us to study the dynamics of the mineralization process and minimizes artifacts during TEM sample preparation. In order to prepare our samples, a drop of aqueous PA (1 mg/ml) was mounted on the holey grid, and the self-assembly of the PA was induced in an atmosphere of HCl vapor. The grids were immersed in aqueous iodine to oxidize the cysteine thiol groups to disulfides. After rinsing with distilled water, these PA coated grids were treated with 5  $\mu$ l of 10 mM CaCl<sub>2</sub> on one side and 5  $\mu$ l of 5 mM Na<sub>2</sub>HPO<sub>4</sub> on the other side. The two solutions are able to mix only by passing through the holes in the carbon support. Grids were examined by TEM at different time intervals (Fig. 3). After 10 min, inorganic material was observed to be concentrated around the fibers, thus increasing their contrast (a crystalline phase was not detected at this time by electron diffraction). At 20 min, the fibers began to be covered with crystalline mineral, although amorphous material remains. After 30 min, plate-shaped polycrystalline mineral is visible throughout the surface of the fibers [Fig. 3C and Web fig. 1 (41)]. The mineral was analyzed by EDS (energy dispersion x-ray fluorescence spectroscopy), which revealed a Ca/P ratio of  $1.67 \pm 0.08$  and is consistent with the formation of HA with a formula of Ca<sub>10</sub>(PO<sub>4</sub>)<sub>6</sub>(OH)<sub>2</sub> (Fig. 3F). In order to discern the relative orientation of the HA crystals with respect to PA fibers, several samples in which isolated mineralized bundles of PA fibers could be observed were analyzed by electron diffraction. In all cases, preferential alignment of the HA crystallographic *c* axis

with the PA fiber long axis was observed (Fig. 3, D and E). In one control, carbon-coated TEM grids were treated as above but in the absence of PA fibers. In this case, no mineral deposit was found on the grids. In a second control, a PA was prepared in which phosphoserine was replaced by serine and treated as above with calcium and phosphate. The nonphosphorylated fibers were observed by TEM after 20 and 30 min of incubation, and in both cases an amorphous mineral deposit around the fibers was observed, but crystals did not form within this time frame [Web fig. 2 (41)].

Our mineralization experiments show that the PA fibers are able to nucleate hydroxyapatite on their surfaces. We designed the nanofibers to have negatively charged surfaces because it is believed that this promotes mineralization by establishing local ion supersaturation (11). In particular, the two acidic amino acids used here, phosphoserine and aspartic acid, are abundant in the proteins of mineralized tissues shown to initiate HA growth (11, 31, 42, 43). The fact that the fibers gain extra electron density before formation of the crystalline phase suggests that local ion supersaturation on the fiber surface may occur in our system. More surprising is the observation that the *c* axes of the HA crystals are co-aligned with long axes of the fibers (Fig. 4). This fact implies that the orientation of crystalline nuclei and the subsequent crystal growth are not random but are controlled by the PA micelles. The exact mechanism of this control is not clear; however, in similar systems, such control is gained by specific arrangement of acidic groups that promote growth of the crystals in a particular orientation by an epitaxial mechanism (3, 7, 11). We may only surmise that an analogous mechanism is used in our system.

The fact that the hydroxyapatite crystals grow with their *c* axes oriented along the long axes of the nanofibers could be of interest in the design of materials, including those used for mineralized tissue repair. This nanoscale organization resembles that of hydroxyapatite crystals in mineralized ECM in which the HA crystals also grow in parallel arrays with their *c* axes aligned with long axes of the organic fibers (2). This arrangement is the most important characteristic of the biominerals belonging to the bone family (1). The organization of the collagen fibers, the porosity, and the mineral-organic ratio vary in different members of this family, yet all are built from the collagen fibrils containing parallel arrays of hydroxyapatite crystals (2, 44, 45).

We have described the self-assembly of discrete nanofibers via a pH-controlled and reversible mechanism. These fibers can be cross-linked by formation of intermolecular disulfide bonds upon oxidation, which results in a chemically robust fiber, and the cross-links can be reversed by the reduction of the disulfides back to free thiol groups. This

highly dynamic system of self-assembly and covalent capture may be easily modified through the selection of different amino acids for other applications in tissue engineering and mineralization. These mineralized nanofibers resemble the lowest level of hierarchical organization of bone in that the crystallographic *c* axis of HA is oriented along the long axis of the organic fibers.

References and Notes

1. S. Weiner, H. D. Wagner, *Annu. Rev. Mater. Sci.* **28**, 271 (1998).
2. W. Traub, S. Weiner, *Proc. Natl. Acad. Sci. U.S.A.* **86**, 9822 (1989).
3. S. Mann, J. P. Hannington, R. J. P. Williams, *Nature* **324**, 565 (1986).
4. D. D. Archibald, S. Mann, *Nature* **364**, 430 (1993).
5. S. L. Burkett, S. Mann, *Chem. Commun.* **9**, 321 (1996).
6. S. I. Stupp, P. V. Braun, *Science* **277**, 1242 (1997).
7. J. Aizenberg, A. J. Black, G. M. Whitesides, *Nature* **398**, 495 (1999).
8. S. R. Whaley, D. S. English, E. L. Hu, P. F. Barbara, A. M. Belcher, *Nature* **405**, 665 (2000).
9. L. Addadi, S. Weiner, *Angew. Chem. Int. Ed. Engl.* **31**, 153 (1992).
10. S. Mann, *J. Chem. Soc. Dalton Trans.* **21**, 3953 (1997).
11. S. Weiner, L. Addadi, *J. Mater. Chem.* **7**, 689 (1997).
12. G. K. Hunter, H. A. Goldberg, *Biochem. J.* **302**, 175 (1994).
13. G. M. Bond, R. H. Richman, W. P. McNaughton, *J. Mater. Eng. Perform.* **4**, 334 (1995).
14. J.-H. Bradt, M. Mertig, A. Teresiak, W. Pompe, *Chem. Mater.* **11**, 2694 (1999).
15. N. Ignjatovic *et al.*, *Biomaterials* **20**, 809 (1999).
16. F. Miyajii, H.-M. Kim, S. Handa, T. Kokubo, T. Nakamura, *Biomaterials* **20**, 913 (1999).
17. H. K. Varma *et al.*, *J. Mater. Sci. Mater. Med.* **10**, 395 (1999).
18. A. Bigi, E. Boanini, S. Panazolva, N. Roveri, *Biomacromolecules* **1**, 752 (2001).
19. M. Kikuchi, S. Itoh, S. Ichinose, K. Shinomiya, J. Tanaka, *Biomaterials* **22**, 1705 (2001).
20. K. Yamada, H. Ihara, T. Ide, T. Fukumoto, C. Hirayama, *Chem. Lett.* **10**, 1713 (1984).
21. Y.-C. Yu *et al.*, *Methods Enzymol.* **289**, 571 (1997).
22. K. C. Lee, P. A. Carlson, A. S. Goldstein, P. Yager, M. H. Gelb, *Langmuir* **15**, 5500 (1999).
23. J. S. Martinez *et al.*, *Science* **287**, 1245 (2000).
24. J. N. Israelachvili, *Intermolecular and Surface Forces* (Academic Press, London, 1992).
25. D. Y. Jackson, D. S. King, J. Chmielewski, S. Singh, P. G. Schultz, *J. Am. Chem. Soc.* **113**, 9391 (1991).
26. T. D. Clark, K. Kobayashi, M. R. Ghadiri, *Chem. Eur. J.* **5**, 782 (1999).
27. Y.-Y. Won, H. T. Davis, F. S. Bates, *Science* **283**, 960 (1999).
28. E. R. Zubarev, M. U. Pralle, L. Li, S. I. Stupp, *Science* **283**, 523 (1999).
29. E. A. Archer, N. T. Goldberg, V. Lynch, *J. Am. Chem. Soc.* **122**, 5006 (2000).
30. F. Cardullo *et al.*, *Chem. Commun.* **5**, 367 (2000).
31. A. George *et al.*, *J. Biol. Chem.* **271**, 32869 (1996).
32. A. Veis, in *Biomineralization: Chemical and Biological Perspectives*, S. Mann, J. Webb, J. R. P. Williams, Eds. (VCH, New York, 1989), pp. 189–222.
33. M. D. Pierschbacher, E. Ruoslahti, *Nature* **309**, 30 (1984).
34. The PA was characterized by <sup>1</sup>H nuclear magnetic resonance (NMR) and MALDI-TOF MS: [M – H]<sup>–1</sup> = 1333.
35. Negatives were digitized in the Umax PowerLook scanner with resolution 1200 dpi. The average thickness of the PA fibers was determined by two different procedures. First, the FTIR of the images and then measurements of the distances between the peaks were performed in the NIH Image 1201.1262 program. The second approach was averaging technique based on the cross-correlation method, widely used in single particle reconstruction, using the EMAN 1201.1202 program. For each data set, 200 to 300 individual square regions were selected.

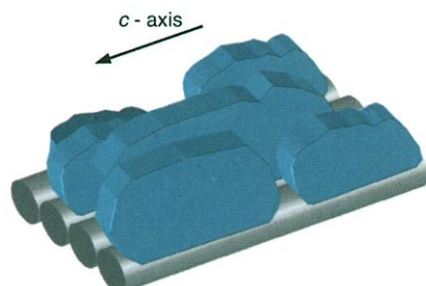


Fig. 4. Scheme showing relations between peptide-amphiphile fibers and hydroxyapatite crystals in the mineralized bundle. Arrow indicates the direction of the *c* axes of the crystals.

36. E. Beniash, W. Traub, A. Veis, S. Weiner, *J. Struct. Biol.* **132**, 212 (2000).
37. J. R. Harris, Ed., *Electron Microscopy in Biology, A Practical Approach* (Oxford Univ. Press, New York, 1991), p. 32 and p. 206.
38. S. Krimm, J. Bandekar, *Adv. Protein Chem.* **38**, 181 (1986).
39. W. K. Surewicz, H. H. Mantsch, D. Chapman, *Biochemistry* **32**, 389 (1993).
40. W. A. Petka, J. L. Harden, K. P. McGrath, D. Wirtz, D. A. Tirrell, *Science* **281**, 389 (1998).
41. Web figures 1 and 2 are available on Science Online at [www.sciencemag.org/cgi/content/full/294/5547/1684/DC1](http://www.sciencemag.org/cgi/content/full/294/5547/1684/DC1).
42. L. Addadi, S. Weiner, *Proc. Natl. Acad. Sci. U.S.A.* **82**, 4110 (1985).
43. G. Falini, S. Albeck, S. Weiner, L. Addadi, *Science* **271**, 67 (1996).
44. S. Weiner, W. Traub, *FASEB J.* **6**, 879 (1992).
45. W. J. Landis, K. J. Hodgins, J. Arena, M. J. Song, B. F. McEwen, *Microsc. Res. Tech.* **33**, 192 (1996).
46. We are grateful for the generous financial support

from DOE (grant no. DE-FG02-00ER45810/A001), NSF (grant no. DMR9996253), and Air Force Office of Scientific Research—Multi University Research Initiative (grant no. F49620-00-1-0283/P01). We would like to thank B. Rabatic for assistance with MALDI-TOF MS, the EPIC center for use of the Hitachi H8100 TEM, the Keck Biophysics Facility for use of the TEM cryo holder, and the Analytical Sciences Laboratory for use of the NMR and FTIR instruments.

6 June 2001; accepted 28 October 2001

## Factors Controlling Long- and Short-Term Sequestration of Atmospheric CO<sub>2</sub> in a Mid-latitude Forest

Carol C. Barford,<sup>1\*</sup> Steven C. Wofsy,<sup>1†</sup> Michael L. Goulden,<sup>2</sup> J. William Munger,<sup>1</sup> Elizabeth Hammond Pyle,<sup>1</sup> Shawn P. Urbanski,<sup>1</sup> Lucy Hutyra,<sup>1</sup> Scott R. Saleska,<sup>1</sup> David Fitzjarrald,<sup>3</sup> Kathleen Moore<sup>3</sup>

Net uptake of carbon dioxide (CO<sub>2</sub>) measured by eddy covariance in a 60- to 80-year-old forest averaged  $2.0 \pm 0.4$  megagrams of carbon per hectare per year during 1993 to 2000, with interannual variations exceeding 50%. Biometry indicated storage of  $1.6 \pm 0.4$  megagrams of carbon per hectare per year over 8 years, 60% in live biomass and the balance in coarse woody debris and soils, confirming eddy-covariance results. Weather and seasonal climate (e.g., variations in growing-season length or cloudiness) regulated seasonal and interannual fluctuations of carbon uptake. Legacies of prior disturbance and management, especially stand age and composition, controlled carbon uptake on the decadal time scale, implying that eastern forests could be managed for sequestration of carbon.

The terrestrial biosphere has sequestered significant amounts of atmospheric CO<sub>2</sub> since 1980, with major contributions from northern mid-latitude forests (1–3). The sink has varied interannually by a factor of 2 or more, correlating with global-scale climate variations (4–6), and may have increased in the 1990s (3). The magnitude of uptake attributed to mid-latitude forests is controversial, however, partly due to sharp disagreement between atmospheric inverse models and forest inventories (7). The cause of net C uptake is also uncertain, with recent studies variously citing land-use change (8, 9), fire suppression (10), longer growing seasons (11), and fertilization by elevated CO<sub>2</sub>

(12) or N deposition (13). These factors must be understood in order to predict growth rates of atmospheric CO<sub>2</sub> and to develop strategies for restraining future increases.

We report here rates of net ecosystem exchange (NEE) of CO<sub>2</sub> for 9 years in a northern hardwood forest (Harvard Forest, 42.5N,

72.2W) measured by using eddy-covariance techniques (14–16). These data are compared with 8 years of biometric measurements of species-specific changes in C storage in live and dead wood, showing where and how the forest is storing C. We determine the C budget and responses to environmental forcing, including diel variations, weather patterns (14), phenology, and interannual climate variability (15). Eddy fluxes may underreport respiration at night in calm winds (17), and methods for removing this bias (18) remain controversial. Here we address possible errors in eddy-covariance data using the biometric data and combine the observations to define the causes of C sequestration and its variation on time scales from hourly to decadal.

Eddy-covariance data extend from 28 October 1991 to 27 October 2000, with valid data for 46,500 of 79,000 hours. Gaps occurred for calibration, data transfer, intense precipitation, maintenance, equipment failure, and weak vertical exchange ( $u^* < 20$  cm s<sup>-1</sup>) (Fig. 1). Ecosystem respiration (R) was observed directly at night and extrapolated for daytime on the basis of day-night changes in soil temperature (18). Gross ecosystem exchange (GEE) was computed from (NEE – R). The 9-year mean annual NEE,  $-2.0$  Mg C ha<sup>-1</sup> year<sup>-1</sup>, is similar to observations at other forested sites in the northeastern United States (19, 20). Annual sums of NEE at this site are insensitive to  $u^*$  within the limits established for valid data (Fig. 1).

Biometric observations of tree growth and

<sup>1</sup>Division of Engineering and Applied Science and Department of Earth and Planetary Science, Harvard University, Cambridge, MA 02138, USA. <sup>2</sup>Department of Earth System Science, University of California, Irvine, CA 92697, USA. <sup>3</sup>Atmospheric Sciences Research Center, University at Albany, State University of New York, Albany, NY 12203, USA.

\*Present address: Center for Sustainability and the Global Environment, Institute for Environmental Studies, University of Wisconsin, Madison, WI 53706, USA.

†To whom correspondence should be addressed. E-mail: [steven\\_wofsy@harvard.edu](mailto:steven_wofsy@harvard.edu)

Fig. 1. Mean annual C uptake from eddy-covariance data versus the hourly-mean value,  $U^*$ , adopted for the minimum friction velocity  $u^*$  [ $\equiv (-\text{momentum flux})^{1/2}$ ] threshold for valid data. Flux values for periods with  $u^* < U^*$  are filled by interpolation (18). Dashed lines show the range of acceptable values for annual NEE ( $2.02 \pm 0.15$  Mg C ha<sup>-1</sup> year<sup>-1</sup>) on the basis of the criteria established in (18). Inclusion of flux data with  $u^* < 17$  cm s<sup>-1</sup> results in underestimation of R. Thresholds of  $u^* > 30$  cm s<sup>-1</sup> leave insufficient flux data for meaningful annual sums.

